

Position reconstruction for segmented detectors

A. Ebrahimi^{a,1}, F. Feindt^a, E. Garutti^a, M. Hajheidari^a, R. Klanner^{a,*}, D. Pitzl^b, J. Schwandt^a,
G. Steinbrück^a, I. Zoi^a

^a*Institute for Experimental Physics, University of Hamburg, Luruper Chaussee 149, 22761 Hamburg, Germany*

^b*DESY, Notkestr. 85, 22607, Hamburg, Germany*

Abstract

The topic of the paper is the position reconstruction from signals of segmented detectors. With the help of a simple simulation, it is shown that the position reconstruction using the centre-of-gravity method is strongly biased, if the width of the charge (or e.g. light) distribution at the electrodes (or photo detectors) is less than the read-out pitch. A method is proposed which removes this bias for events with signals in two or more read-out channels and thereby improves the position resolution. The method also provides an estimate of the position-response function for every event. Examples are given for which its width as a function of the reconstructed position varies by as much as an order of magnitude.

A fast Monte Carlo program is described which simulates the signals from a silicon pixel detector traversed by charged particles under different angles, and the results obtained with the proposed reconstruction method and with the centre-of-gravity method are compared. The simulation includes the local energy-loss fluctuations, the position-dependent electric field, the diffusion of the charge carriers, the electronics noise and charge thresholds for clustering. A comparison to test-beam-data is used to validate the simulation.

Keywords: Position reconstruction, segmented detectors, simulation of Si pixel detectors, centre-of-gravity method, position resolution.

Contents

1	Introduction	2
2	Method	2
3	Angular dependence of the charge distribution at the electrode plane	6
4	Signal simulation of signals in a pixel sensor	7
5	Energy-loss fluctuations and position resolution	7
6	Position resolution of silicon pixel sensors	8
6.1	Position resolution as function of threshold for track angles between 0° and 32°	8
6.2	Comparison of simulation results on cluster size and position resolution to test-beam data	12
7	Summary and conclusions	15

¹Now at Paul Scherrer Institut, 5232 Villigen, Switzerland.

*Corresponding author, Email address: Robert.Klanner@desy.de, Tel.: +49 40 8998 2558.

A Appendices	15
A.1 Signal simulation	15
A.2 Energy loss simulation	17
A.3 Spatial distribution of tracks over the electrode pitch	18

1. Introduction

The position reconstruction using analogue signals from segmented detectors is a standard analysis problem. Frequently the "centre-of-gravity" method for clusters of signals exceeding a threshold is used, which is simple and robust, but results in most cases in a biased position reconstruction [1, 2]. "Bias" means that x_{true} , the position at which particles hit the detector, and $\langle x_{rec} \rangle$, the mean reconstructed position for a given x_{true} differ. This paper describes a general method which can be used to correct such a bias for a given position-reconstruction algorithm, and also determine the position-response function, i. e. the probability-density distribution of Δx , where Δx is the difference between true and reconstructed position. The method does not require additional data beyond those to be reconstructed.

Compared to methods reported in the literature and discussed in more detail in the conclusions of Sect. 2, the proposed method is simpler to implement: It does not require the selection of a fixed cluster size, which has to be adjusted as a function of the track angle, nor an externally predicted position. The position resolution achieved by the proposed method is similar to reconstruction methods described in the literature.

To demonstrate the method, Monte Carlo data are analysed, which simulate the signals from silicon pixel sensors for minimum ionizing particles at different incident angles, and the resolutions using the "centre-of-gravity" and the proposed method are compared. The validity of the simulated data is verified by a comparison to test-beam data taken with three parallel pixel detectors with a pixel pitch of $25 \mu\text{m} \times 100 \mu\text{m}$. In addition, the expected improvement of the position resolution for the test-beam data as a function of track angle is presented. It is noted that the method is not limited to the centre-of-gravity algorithm, but can be used for other reconstruction methods.

The paper is structured in the following way. In the next section a simple model for the signals from strip detectors is used to explain the reason of the bias of the centre-of-gravity method, and a reconstruction method which avoids this bias is developed. This is followed by a discussion of the effects of charge-carrier diffusion on the charge distribution arriving at the electrodes for charged particles traversing a silicon strip detector at different angles. A short description of the Monte Carlo program used to simulate the signals in silicon pixel detectors follows. Next, the fluctuations of the mean position of the charge distribution at the electrodes due to the fluctuations of the energy loss along the particle track is presented. In Sect. 6, simulations of the signals from a pixel silicon sensors for track angles of 0° , 10° , 20° and 32° are used to study the position resolution as a function of the threshold used to assign signals to a cluster. Finally, the results of the simulations are compared to test-beam data for track angles between 0° and 30° , and the expected improvement in position resolution of the proposed method compared to the centre-of-gravity algorithm presented. Sect. 7 summarizes the results. The Appendices give details of the Monte Carlo program used, and presents a method for determining the average distribution of tracks in the pixels from the measured distribution of particles over the entire sensor.

2. Method

The method of correcting the bias of a given reconstruction algorithm, is explained with the help of Fig. 1, which shows a strip detector with 3 readout channels of pitch p . The signal distributions, dQ/dx , at the electrode plane by two particles at normal incidence are shown as solid lines. The signal, Q_i , collected by strip i is given by the integral of dQ/dx over the corresponding strip pitch. A reconstruction algorithm is used to obtain the reconstructed position, x_{rec} , from the Q_i . Frequently, the centre-of-gravity is used for which $x_{rec} = \sum(c_i \cdot Q_i) / \sum Q_i$, where the c_i are the positions of the strip centres.

To illustrate the proposed method, 10^6 Monte Carlo events are generated in the following way: The strip pitch is $p = 25 \mu\text{m}$, and the signal distribution, dQ/dx , is simulated by the sum of two normalized Gauss-distributed random numbers with weights 1/2, mean values x , and $\sigma = 2$ and $5 \mu\text{m}$, respectively.

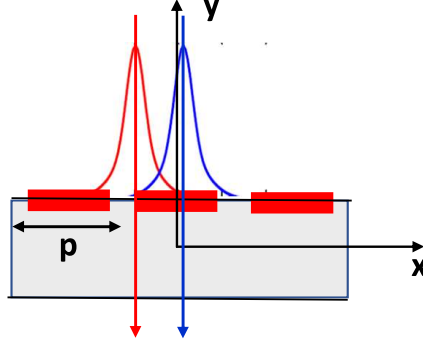


Figure 1: Sketch of a detector with three readout strips with pitch $p = 25 \mu\text{m}$. The charge distributions, dQ/dx , induced by two particles with normal incidence, one at $x = -10 \mu\text{m}$ and the other at $1 \mu\text{m}$, are shown; $x = 0$ is at the centre of the central strip. Independent of the x position of the particle the charge distribution induced at the electrode plane, dQ/dx , is simulated by two Gauss functions with equal weights, one with $\sigma = 2 \mu\text{m}$ and the other with $\sigma = 5 \mu\text{m}$. This simple model is only used to demonstrate the method. For a more realistic model we refer to Sect. 4 and Appendix A.1.

For the position x , a uniformly distributed random number in the range $-p/2 \leq x < p/2$ is generated, and the signal Q_i of strip i is obtained by integrating dQ/dx over the strip pitch. To account for noise, Gauss-distributed random numbers with $\sigma_{el} = 0.025$ are added to the Q_i . This very simple simulation approximates the response of a silicon strip sensor with $25 \mu\text{m}$ pitch in the x direction, to particles with normal incidence uniformly distributed in x over the pitch of the central strip. It is used to explain the method and allows for analytical calculations for checking the analysis code. The widths of the Gaussians, $\sigma = 2 \mu\text{m}$ and $5 \mu\text{m}$, correspond to charge collection times for electrons of 0.6 and 3.6 ns, which are typical for different regions in thin silicon detectors. For the detailed studies and the comparison to experimental data, the more realistic simulation of pixel sensors presented in Sect. 4 is used.

In Fig. 2a the event distributions of dN/dx for x_{true} and x_{rec} are shown. The generated x position is denoted x_{true} , and the position reconstructed with the centre-of-gravity method without threshold cuts x_{rec} . The generated distribution dN/dx_{true} is flat, whereas dN/dx_{rec} peaks at $x_{rec} = 0$. The reason is that the signal distribution at the strips, dQ/dx , peaks at the track position x_{true} which biases the x_{rec} values towards $x_{rec} = 0$. It is noted that only for flat signal distributions with widths, which are multiples of p , the centre-of-gravity has no bias. Removing the bias means finding the function $x_{corr}(x_{rec})$ so that dN/dx_{corr} is a flat distribution of width p , i.e. has the same shape as dN/dx_{true} .

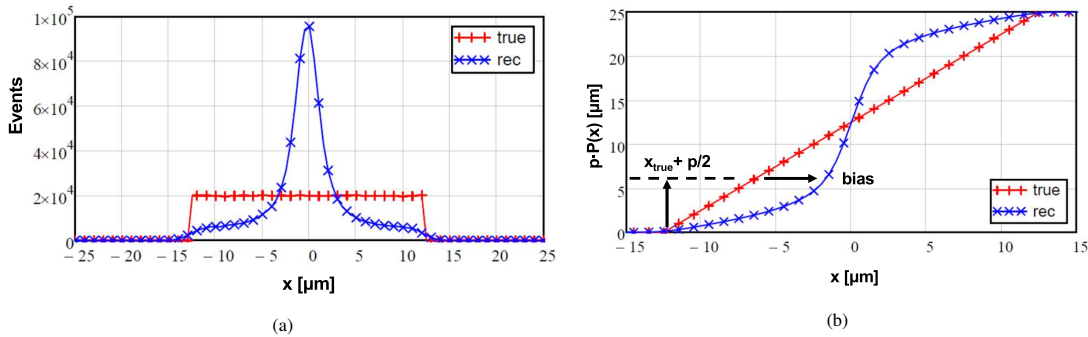


Figure 2: (a) Distributions dN/dx within an electrode of width $p = 25 \mu\text{m}$ for x_{true} and the reconstructed position x_{rec} . (b) Normalised cumulative distributions of the curves shown in (a) multiplied with p . The horizontal arrow shows the mean bias used to correct x_{rec} .

This can be achieved by using the normalized cumulative distributions

$$P_{true}(x) = \frac{1}{N_{tot}} \int_{-p/2}^x (dN/dx_{true}) dx_{true} \quad \text{and} \quad P_{rec}(x) = \frac{1}{N_{tot}} \int_{-p/2}^x (dN/dx_{rec}) dx_{rec}. \quad (1)$$

Fig. 2b shows $p \cdot P_{rec}(x)$ and $p \cdot P_{true}(x)$. The mean bias, $\langle x_{rec} - x_{true} \rangle$ is obtained from $P_{rec}(x_{rec}) =$

$P_{true}(x_{true} - x_{rec})$, which follows from the requirement of equal number of events between $-p/2$ and x_{true} for dN_{true}/dx , and between $-p/2$ and x_{rec} for dN_{rec}/dx . For a uniform dN/dx_{true} , $P_{true}(x)$ is the diagonal between $x = -p/2$ and $x = p/2$, and

$$x_{corr} = p \cdot (P_{rec}(x_{rec}) - 0.5). \quad (2)$$

For a non-uniform dN/dx_{true} , the horizontal distance shown in Fig. 2b has to be used. However, as shown in the Appendix A.3, for most situations the assumption of a flat x_{true} is valid. Using Eq. 2, x_{corr} can be calculated on an event-by-event basis, and the $(x_{corr} - x_{true})$ distributions for events in x_{corr} intervals are estimates of the x_{corr} -dependent response functions of the position determination.

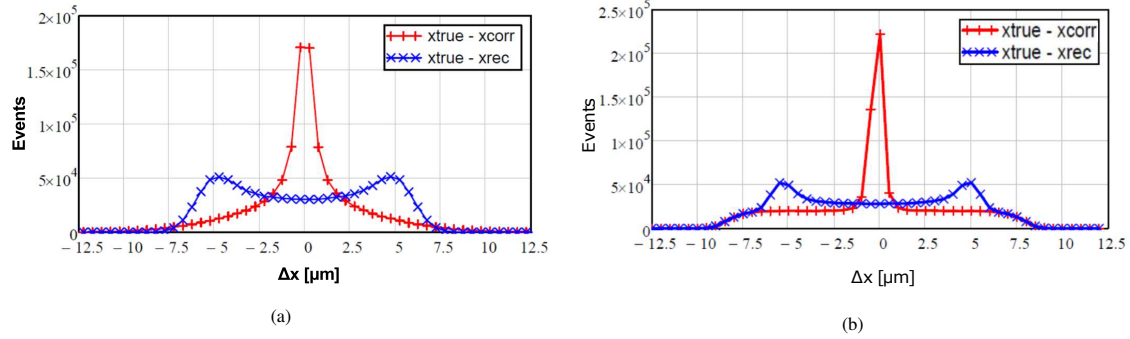


Figure 3: Distributions of Δx for x_{rec} and x_{corr} for the simulated events described in the text. (a) Without, and (b) with a threshold cut at 10% of the mean signal.

To illustrate the improvement of the position determination by the correction method, Fig. 3a shows the residual distributions $\Delta x_{rec} = x_{true} - x_{rec}$ and $\Delta x_{corr} = x_{true} - x_{corr}$. A significant improvement is seen, which is mainly caused by the events in the region of the boundaries between electrodes. These events have a very good spatial resolution, however they are reconstructed with a bias of up to $5 \mu\text{m}$ by the centre-of-gravity method and produce the enhancements at $|\Delta x_{rec}| \approx 5 \mu\text{m}$. It is noted that the position-response function is very different from a Gauss function.

So far, x_{rec} has been obtained from the Q_i without threshold cuts. As a result, for events in which most of the charge is induced in the central strip, the contribution of the signal in the adjacent strips is dominated by random noise and thus worsens the position resolution. In the following the effect of threshold cuts will be discussed. For the study, the simulated events discussed above with a threshold cut, $thr = 4 \cdot \sigma_{el} = 0.1$ for a mean total signal of $\sum Q_i = 1$ is used. Threshold cuts result in events with different cluster sizes, cls . The cluster-size distribution $dN/dcls$ depends on the track angle θ and so does the optimal algorithm for x_{rec} [3].

Depending on cls , the value for x_{rec} differs:

$$\begin{aligned} cls = 0 & \quad x_{rec} \text{ no information available} \\ cls = 1 & \quad x_{rec} = 0 \\ cls > 1 & \quad x_{rec} \text{ from a reconstruction algorithm} \end{aligned}$$

In order to assure that dN/dx_{true} for the events for which x_{rec} can be calculated remains flat, the fraction of events with $cls = 0$ (inefficiency) has to be small. For the simulated events the fractions of events with $cls = 0, 1, 2$, and 3 are $0, 63.5\%, 36.5\%$, and $10^{-3}\%$, respectively. Fig. 4a shows the distributions dN/dx_{true} and dN/dx_{rec} for different cls . The 6.35×10^5 $cls = 1$ events cover the central region of x_{true} and are reconstructed at $x_{rec} = 0$. The 3.65×10^5 $cls = 2$ events cover the outer region of x_{true} . Their x_{rec} values are shifted towards the centre because of the bias of the centre-of-gravity algorithm. Because of the $thr = 0.1$ cut, no $cls = 2$ events are reconstructed in the region $|x_{rec}| \lesssim 2.5 \mu\text{m}$. Fig. 4b shows the normalised cumulative distributions, $P_{true}(x)$ and $P_{rec}(x)$, multiplied with p , with the bias correction according to Eq. 2 indicated by the arrow. This correction can only be applied to the $cls > 1$ events. Fig. 3b compares the $(\Delta x_{rec} = x_{true} - x_{rec})$ - with the $(\Delta x_{corr} = x_{true} - x_{corr})$ -distribution. Similar to the situation without threshold cut shown in Fig. 3a, a significant improvement of the position resolution is observed: Although for $thr = 0.1$ only 36.5% of the events have $cls = 2$, the rms of the Δx distributions decreases

from $4.5 \mu\text{m}$ for the centre-of-gravity method to $3.7 \mu\text{m}$. The $cls = 2$ events, which cause the peaks around $|x_{true} - x_{rec}| = 5 \mu\text{m}$ are moved to the narrow peak at $x_{true} - x_{corr} = 0$, whereas the $cls = 1$ events cause the flat distribution below the peak. It should be noted that decreasing thr , increases the fraction of $cls = 2$ events and improves the overall position resolution: The rms of the Δx_{corr} distribution is $2.7 \mu\text{m}$ for a threshold $thr = 0.04$. It is noted that the position resolution has a strong dependence on the particle position relative to the strip centre.

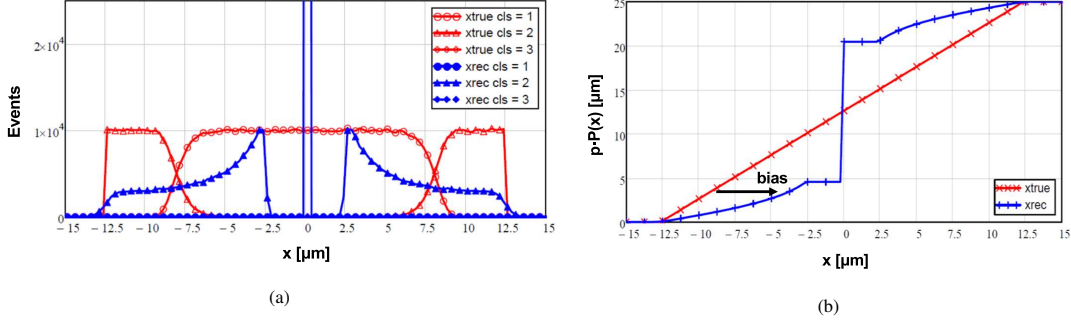


Figure 4: Results of the analysis of the simulated data with a threshold cut of 0.1. (a) Event-number distribution dN/dx for different cluster sizes, cls , for x_{true} and for x_{rec} . The δ function peak at $x = 0$ comes from the $cls = 1$ events. (b) Normalised cumulative distributions of the distributions shown in (a) multiplied with p . The horizontal arrow shows the bias used to correct x_{rec} for $cls > 1$.

Next the question is addressed, if the correction depends on the charge, Q , generated by the particle. This is studied by varying the threshold, thr , for a fixed Q . Fig. 5a shows the normalised cumulative distributions, P_{rec} , for $thr = 0, 0.06$ and 0.1 . As expected for the charge-sharing region $|x_{rec}| \geq 2.5 \mu\text{m}$, P_{rec} is independent of thr . A decrease of thr increases the fraction of events with $cls > 1$, decreases the step at $x = 0$, and extends the continuous region of P_{rec} to smaller $|x_{rec}|$ values. The study suggests that for energetic charged particles, where Q follows a Landau distribution, a single correction function can be used as long as no energetic δ -electrons are produced.

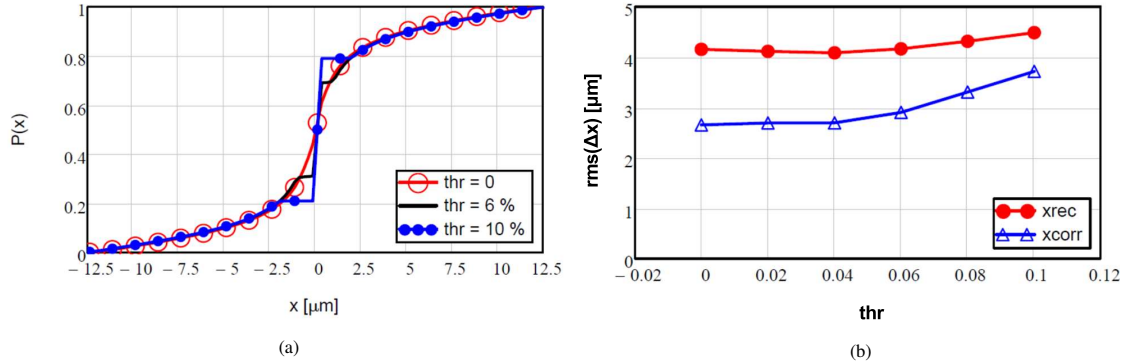


Figure 5: (a) Normalized cumulative distribution, $P(x)$, for 3 threshold values, thr . (b) rms values of the overall resolution for x_{rec} , the position reconstructed with the centre-of-gravity method, and for x_{corr} , the position corrected for bias for events with cluster size $cs \geq 2$ as a function of thr .

Fig. 5b compares rms_{rec} , the root-mean-square of the resolution for normal incidence for x_{rec} , the position reconstructed by the centre-of-gravity method, with rms_{corr} using the proposed method, as a function of thr . A significant improvement is observed, which decreases with increasing thr , because of the increase of events with $cls = 1$.

To summarize this section: A method which corrects the bias of position-reconstruction algorithms for segmented detectors with analogue readout is proposed. The method is explained and demonstrated with the help of a very simple simulation of charged particles traversing a silicon strip detector at normal incidence using the centre-of-gravity algorithm for the position reconstruction. It is shown that the proposed method

corrects the bias of the centre-of-gravity algorithm for events with $cls > 1$, and achieves a significant improvement of the spatial resolution for the simulated data. The method can also be used for other reconstruction methods.

The method is similar to the η algorithm of Refs. [1, 3]: For $cls \leq 1$ there is insufficient information for any correction, for $cls = 2$ both methods are identical, and for $cls > 2$ the proposed algorithm automatically performs the bias correction independent of the reconstruction method, whereas for the η algorithm it has to be decided how to assign measured charges to what is called the *RIGHT* and the *LEFT* signal in Ref. [1]. An extension of the η algorithm, the *multi-pixel η -correction* (mp- η) is presented in Ref. [4]. The only difference to the correction method used in this paper is that the method is applied to fixed read-out patterns, and thus a fixed cluster size. Therefore, it can not be used if only signals above a fixed threshold are recorded, which results in different cluster sizes. In Ref. [5] an η corrections for the individual cluster sizes is applied. The method requires the knowledge of Δ_{cls} , the widths of the regions in pixel coordinates producing clusters of size cls . For fully depleted detectors with high charge collection efficiency, the calculation of Δ_{cls} is straight forward. However, for highly-irradiated detectors with significant charge losses, in particular if they have depletion regions on both front and rear side with a non-depleted region in between, it is not clear how to estimate Δ_{cls} . The step shown in Fig. 4b actually determines $\Delta_{cls=1}$, however this information is not used by the authors. Examples for other bias-correction methods are given in Refs. [6, 7, 8], where the corrections are derived from the difference in track position predicted by a beam telescope and the one measured in the detector under study. The mean of the difference distribution as a function of the predicted position in the sensor is fitted by a fifth-order polynomial. This method achieves a similar performance as the η algorithm.

It is concluded: The method presented does not achieve a higher precision than previously used methods, but it is more easily implemented and does not require additional information beyond the signals recorded in the individual detector elements.

3. Angular dependence of the charge distribution at the electrode plane

In this section the effect of diffusion on the charge distribution arriving at the electrode plane is investigated using a simple calculation. Shown are the charge distributions, dQ/dx , for particles passing through the centre with angles $\theta = 0^\circ$, 10° and 20° to the sensor normal. For simplicity a uniform charge distribution without fluctuations along the particle track is assumed.

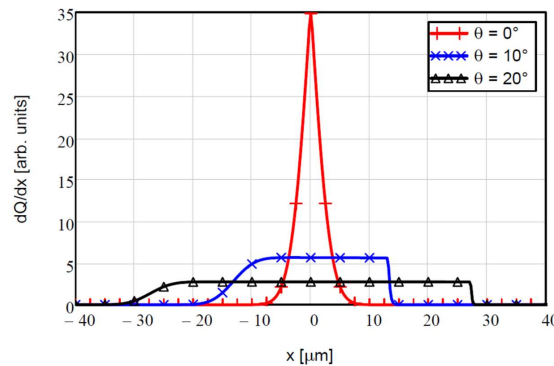


Figure 6: Simulated charge distributions, dQ/dx induced at the electrode plane for particles passing through the centre of a $150 \mu\text{m}$ thick sensor at angles of $\theta = 0^\circ$, 10° and 20° to the sensor normal. For finite angles $\theta > 0^\circ$ the drop of dQ/dx to zero for negative x is shallower than for positive x , as in the former case the charges which reach the electrodes have to drift through the entire sensor, which results in an increased diffusion. The temperature used for the calculation is 20°C .

The calculation of the charge distribution induced in the electrode plane for a sensor of thickness $d = 150 \mu\text{m}$ and p -doping density $4 \times 10^{12} \text{cm}^{-3}$ at $T = 20^\circ\text{C}$ takes into account the electric field in the sensor and the diffusion of the electron cloud. For the coordinate system of Fig. 1, dQ/dx is obtained by integrating Gauss distributions with mean positions $\mu(y) = y \cdot \tan(\theta)$ and rms widths $\sigma(y)$ from Eq. 4 of Appendix A.1 between $y = -d/2$ and $y = d/2 - \epsilon$. $\epsilon = 0.1 \mu\text{m}$ is introduced to avoid the divergence due

to $\sigma(y = d/2) = 0$. The results of the calculation are shown in Fig. 6. As expected, for angles θ different from zero, the full width at half maximum of the dQ/dx distribution is $d \cdot |\tan(\theta)|$. For $\theta > 0^\circ$, the drop of dQ/dx to zero is shallower for negative x than for positive x . The reason is that in the former case the electrons drift through the entire detector, whereas in the latter one their drift distance is close to zero. The increased drift time results in an increased spread of the electron cloud by diffusion.

As a result a threshold used for the cluster selection will affect the two regions differently and cause a bias for the reconstructed position, x_{rec} . Thus even for the optimal angle, $\theta = \text{atan}(p/d)$, where the width of the dQ/dx distribution is equal to the electrode pitch p , the centre-of-gravity reconstruction is biased. However, as shown in Sect. 6.1, the effect is small, but the proposed correction method corrects for this bias, too.

4. Signal simulation of signals in a pixel sensor

In Sect. 2 a highly simplified model for a silicon strip sensor has been used to explain the proposed position-reconstruction method and illustrate some of its features. The model has the advantage that for most results analytical calculations can be used to verify the analysis. In this section a significantly more realistic model for a pixel sensor is introduced, which is used for more detailed investigations and a comparison to experimental results. Details of the model and of its implementation are given in the Appendices.

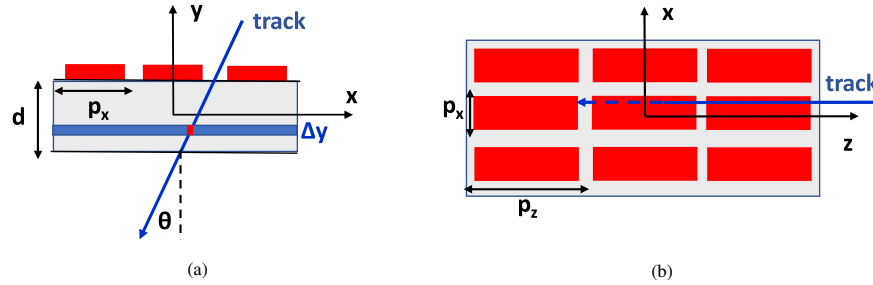


Figure 7: Sketch of the simulated sensor and illustration of the coordinate system. The simulated tracks are uniformly distributed over the central pixel and located in the $x - y$ plane with an angle θ to the y axis. (a) Cross section, and (b) top view.

Fig. 7 shows a cross section and a top view of the simulated pixel sensor and a track traversing the central pixel. The track is in the $x - y$ plane with an angle θ relative to the y axis. For the electric field the 1D-field of a pad sensor of thickness, d , with constant doping, and a bias voltage above full depletion is assumed. For the simulation, the sensor is segmented into n_y segments of equal thickness, Δy . For every segment a random number corresponding to the energy loss of a 5 GeV particle for a track length $\Delta y/\cos(\theta)$ is generated and the corresponding charge assigned to the centre of the segment. The energy loss model of Bichsel [9] is implemented and details are given in Appendix A.2. The electron clouds generated in the individual Δy segments are drifted to the readout plane, taking into account the effects of diffusion. Their spatial distribution at the readout plane is integrated over the x and the z pitch of the pixels for obtaining the charges in the individual pixels. Electronics noise, threshold cuts and position reconstruction are performed in the analysis of the simulated events. The simulation program generates approximately 500 k events in one minute on a standard PC.

5. Energy-loss fluctuations and position resolution

In this section the worsening of the position resolution with track angle due to local energy-loss fluctuations is investigated. The Monte Carlo program discussed in the previous section is used to generate for tracks with $x = z = 0$ the energy deposited in the n_y segments, and the energy-weighted mean position, $\langle y \rangle$, is calculated for every simulated event. The event-to-event fluctuations of $\langle y \rangle$ multiplied with $\sin(\theta)$ are an estimate of the contribution of the energy-loss fluctuations to the spatial resolution. Results of 10^6 events for a $150 \mu\text{m}$ thick detector and $n_y = 15$ and θ between 0° and 50° are shown in Fig. 8. Fig. 8a shows the energy lost in the entire sensor which increases with θ because of the $\propto 1/\cos(\theta)$ increase in path length. In

Fig. 8b the width of the distribution of $\Delta x = \langle y \rangle \cdot \sin(\theta)$, which results from the position-dependent energy losses, is displayed. As shown in Fig. 9, the distribution of the fluctuations has significant non-Gaussian tails due to infrequent large local energy losses. Therefore, both the root-mean square, rms , and the full width at half maximum, Γ , are presented. It has been verified that for $n_y \geq 10$ the results do not depend on n_y . It is noted that the finite range of δ -electrons is not taken into account in the simulation and their energy is deposited locally; δ -electrons cause an additional broadening of the Δx distribution.

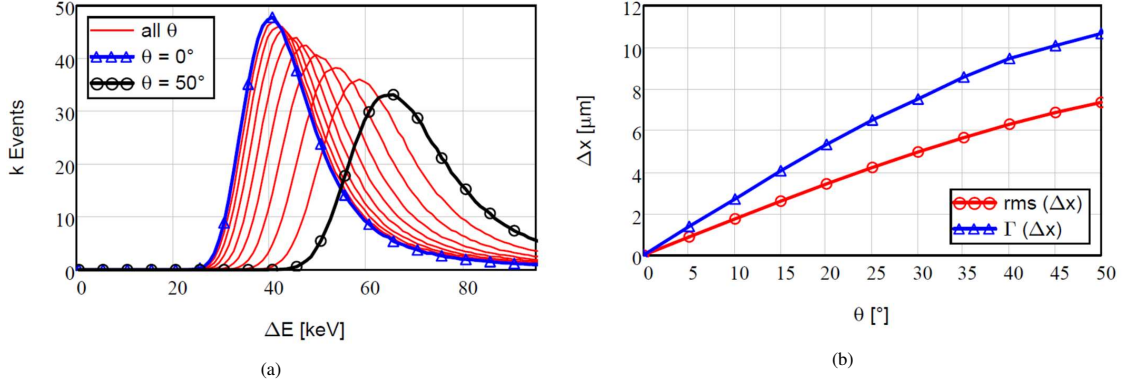


Figure 8: (a) Simulated $dN/d\Delta E$ distribution for track angles between 0° and 50° in steps of 5° . (b) Contribution of the fluctuations of the deposited energy, $\Delta E (y)$, to the position resolution for track angles between 0° and 50° . As the distribution has non-Gaussian tails, both the rms and the full width at half maximum, Γ , are shown. An example of the effect of the tails on the rms : For $\theta = 45^\circ$, $\Gamma = 10 \mu\text{m}$. The corresponding rms for a Gaussian is $\sigma = \Gamma/2.35 = 4.3 \mu\text{m}$, whereas $rms = 6.8 \mu\text{m}$ for the simulated Δx distribution shown in Fig. 9. The additional broadening due to the finite range of δ -electrons is not taken into account in the simulation.

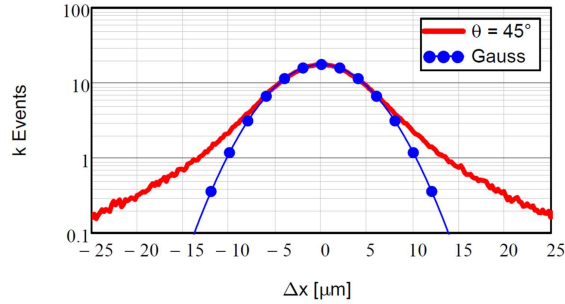


Figure 9: Influence of the local energy-loss fluctuations on the position resolution of segmented Si detectors; Δx , is the difference between the generated particle position and the centre-of-gravity of the charge distribution at the electrodes for a particle incident with an angle $\theta = 45^\circ$ on a $150 \mu\text{m}$ thick sensor. To illustrate the non-Gaussian tails, the result of the simulation (solid line) is compared to a Gauss distribution with the same full width at half maximum (line with markers).

It is concluded that for a $150 \mu\text{m}$ thick detector at angles above 10° the contribution of the local fluctuations of energy loss to the spatial resolution can be important, and algorithms, like the head-tail algorithm [3], which ignore the charge measured in the central electrode for large clusters, typically give superior results than the centre-of-gravity method.

6. Position resolution of silicon pixel sensors

6.1. Position resolution as function of threshold for track angles between 0° and 32°

In this section the spatial resolution for the centre-of-gravity algorithm and the method described in Sect. 2 is compared for four angles in the range $\theta = 0^\circ$ to 32° , as a function of the threshold used for the cluster reconstruction. The sensor parameters for the simulation, defined in table 1 of Appendix A.1, are: $d = 150 \mu\text{m}$, $p_x = 25 \mu\text{m}$, $p_z = 100 \mu\text{m}$, $n_{pz} = 3$, $n_y = 15$, $\Delta x_{min} = 2 \mu\text{m}$, $N_d = 4.5 \times 10^{12} \text{cm}^{-3}$,

$U = 150$ V, $\sigma_{el} = 275$ e (elementary charges), $\Delta E_{max} = 2$, and $T = 20$ °C. The parameters correspond to prototype sensors developed for the luminosity upgrade of the CMS Inner Tracker [10]. For $\theta = 0^\circ$ and 10° , n_{px} is set to 3, and for the larger angles to 5, to account for the increase of the width of the charge distribution collected by the pixels with θ . The threshold, thr , for assigning signals to a cluster is varied between 0 and 1100 e (elementary charges) in steps of 220 e, corresponding to 0, 2%, 4% up to 10% of the most probable value of the charge distribution from the entire sensor at normal incidence ($MPV = 11\,000$).

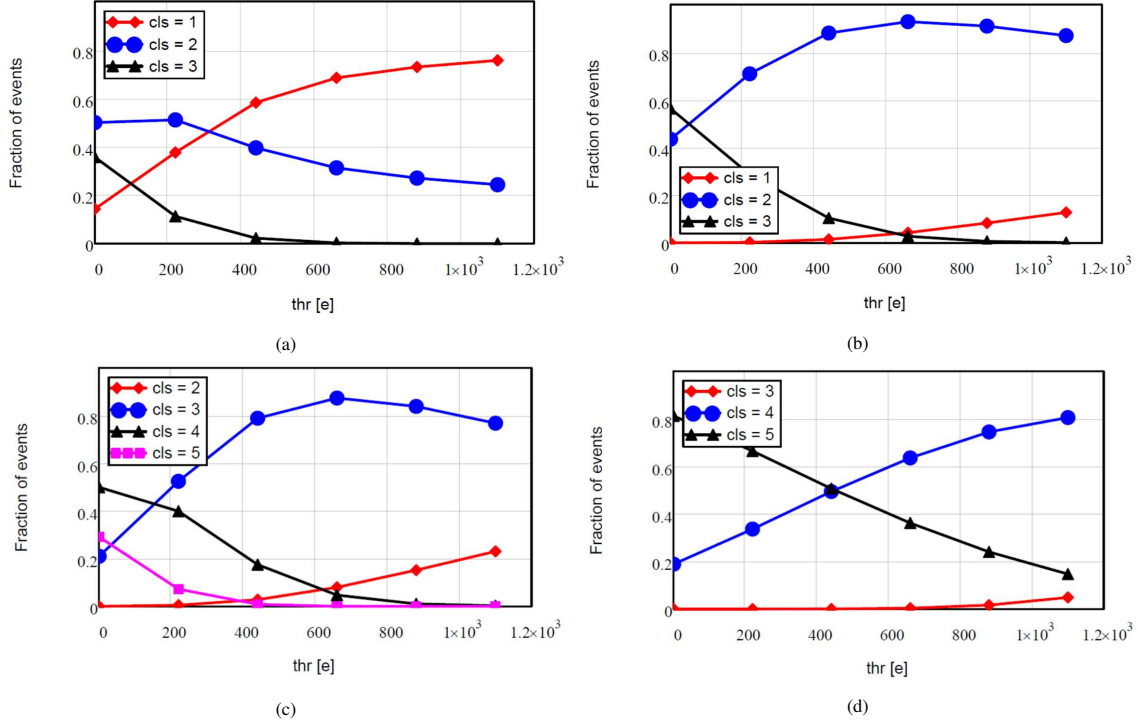


Figure 10: Fraction of events with cluster size $cls = 1$ to 5 as a function of threshold, thr , for tracks with angles of (a) 0° , (b) 10° , (c) 20° , and (d) 32° to the sensor normal. The threshold is given in units of elementary charges, e, and the most probable signal charge at 0° is $\approx 11\,000$ e.

Fig. 10 shows the fraction of events with different projected cluster sizes, cls , as a function of threshold, thr for the four θ values. The cluster size cls is obtained by adding the signals with the same z values and counting only those which are above thr . For $\theta = 0^\circ$ and $thr \geq 400$ e the $cls = 1$ events, for $\theta = 10^\circ$ the $cls = 2$ events, and for $\theta = 20^\circ$ the $cls = 3$ events dominate. For $\theta = 32^\circ$, most events have $cls = 4$ for small and $cls = 3$ for large thr .

In Fig. 11 the x distribution of the simulated events reconstructed with the centre-of-gravity algorithm, x_{rec} , and with the method discussed in Sect. 2, x_{corr} , are compared to the flat x_{true} distributions generated. The distributions for the $thr = 2\%$ to 8% values are shown as narrow lines, the ones for 0 and 10% with symbols.

Figs. 11a and 11b show the comparison for $\theta = 0^\circ$. For $cls = 1$, both x_{rec} and x_{corr} are reconstructed at $x = 0$. The $x = 0$ bins are cut off in the histograms, so that the remaining events are visible on a linear scale. The regions adjacent to $x = 0$ are depleted of events, with a gap which increases with thr , as already discussed in Sect. 2. For $cls = 2$ and x_{rec} the number of events reconstructed at higher $|x|$ values are much smaller than the ones generated: They are reconstructed at $|x_{rec}| \ll |x_{true}|$. As shown in Fig. 11b the proposed method is able to correct this.

The comparison for $\theta = 10^\circ$ are shown in Figs. 11c and 11d. For $\theta = 10^\circ$ and $thr \geq 400$ e about 90% of the events have $cls = 2$ (Fig. 10b), and the number of events in the $x = 0$ bin is reduced to about 10%. For the centre-of-gravity reconstruction, the $cls = 2$ events are reconstructed correctly on average, however their x distribution shows a complicated structure. The asymmetry for small $|x_{rec}|$ values is caused by the diffusion effect discussed in Sect. 3. The deviations at $|x_{rec}| \approx p_x/2$ are mainly caused by electronics noise

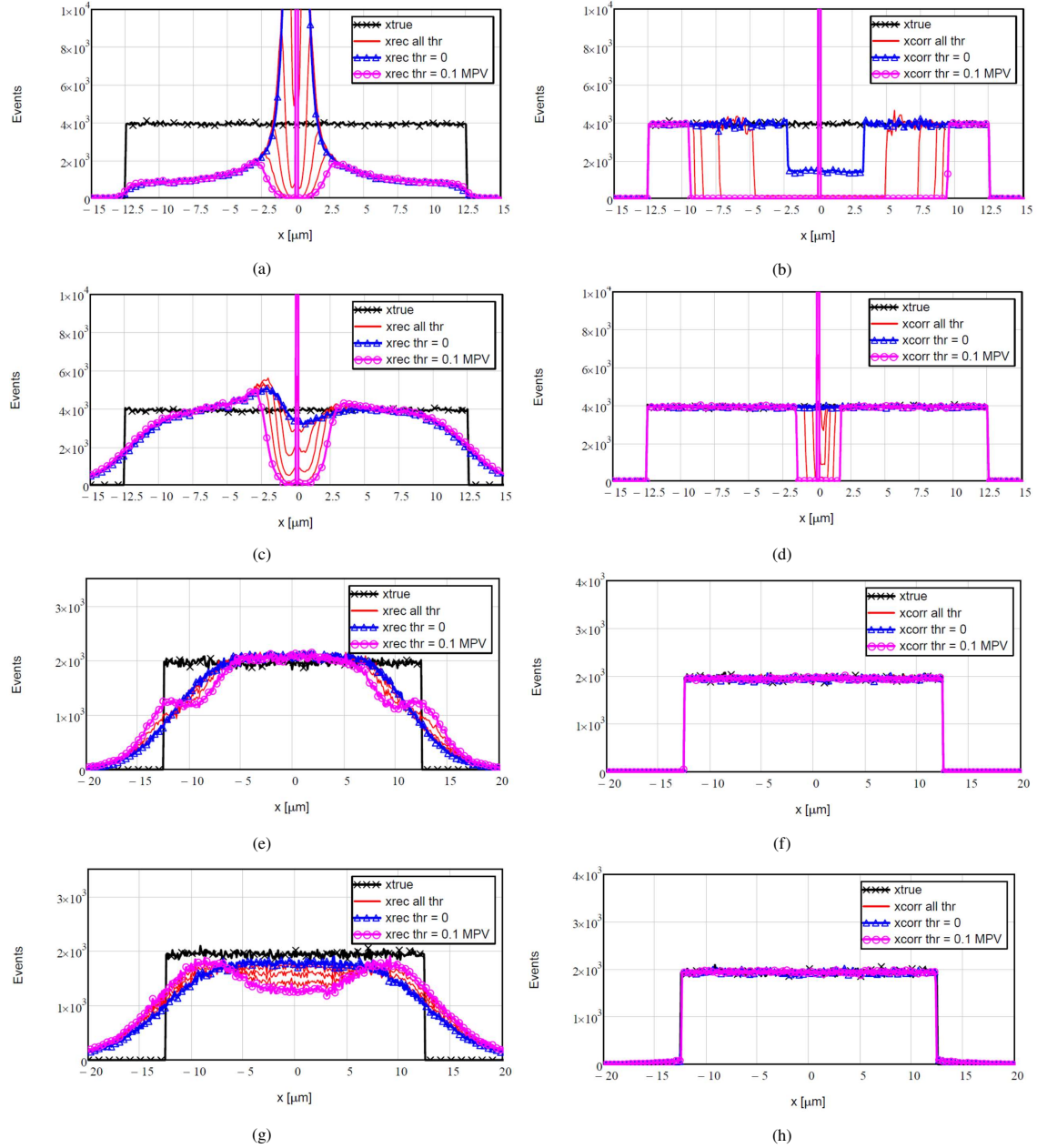


Figure 11: Distributions dN/dx_{rec} , as a function of thr for (a) $\theta = 0^\circ$, (c) 10° , (e) 20° , (g) 32° , and of dN/dx_{corr} for (b) $\theta = 0^\circ$, (d) 10° , (f) 20° , (h) 32° . The thin red lines show the distributions for $thr = 2, 4, 6$, and 8% of the most probable value (MPV) of the charge distribution for $\theta = 0^\circ$, and thicker ones for $thr = 0$ and 10% .

and the bias of the reconstruction method. The proposed method manages to reproduce the flat distribution of the generated events. Although it is expected to correct for the asymmetric bias in the central region, it can not correct for the effects of random electronics noise for $|x| \approx p_x/2$. Thus only a minor improvement of the position resolution can be expected. Similar observations are made for the $\theta = 20^\circ$ and $\theta = 32^\circ$ results.

Fig. 12 shows the position-response functions, $dN/d\Delta x$, for $\Delta x_{rec} = x_{true} - x_{rec}$ and for $\Delta x_{corr} = x_{true} - x_{corr}$ of the data shown in Fig. 11. In the literature Δx is frequently called *residual*.

For $\theta = 0^\circ$ (Fig. 12a) the Δx_{rec} distributions show peaks at $|\Delta x| \approx 7 \mu\text{m}$. They originate from $cls = 2$ events, which are reconstructed at too small $|x|$ values. They are absent in the Δx_{corr} distribution

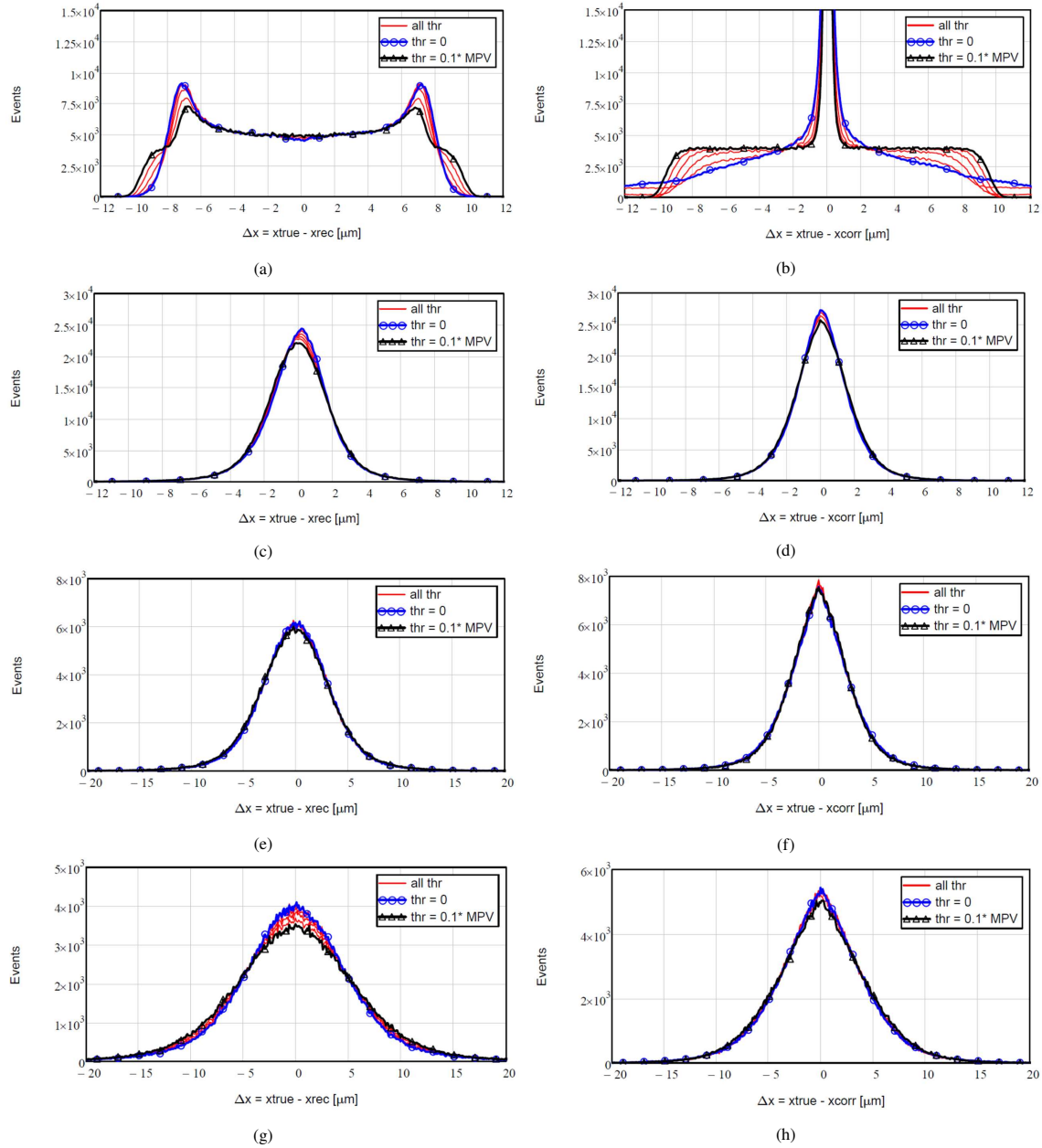


Figure 12: Distributions of the differences $\Delta x = x_{true} - x_{rec}$ as a function of thr for (a) $\theta = 0^\circ$, (c) 10° , (e) 20° , (g) 32° , and of $\Delta x = x_{true} - x_{corr}$ for (b) $\theta = 0^\circ$, (d) 10° , (f) 20° , (h) 32° . The thin red lines show the distributions for $thr = 2, 4, 6,$ and 8% of the most probable value (MPV) of the charge distribution for $\theta = 0^\circ$, and thicker ones for $thr = 0$ and 10% .

(Fig. 12b). The $cls = 2$ events appear in a narrow peak at zero, and actually represent the events with the best position resolution. The flat part of the Δx_{corr} distributions comes from the $cls = 1$ events. For higher thr values the fraction of $cls = 1$ events increases and the flat part extends to higher $|\Delta x_{corr}|$ values. For lower thr values the fraction of the $cls = 2$ events due to electronics noise increases, and higher $|\Delta x_{corr}|$ values appear. Therefore there will be an optimal value of thr . This can be seen in Fig. 13a, which shows the rms of the Δx distributions. At the optimal value, $thr \approx 660$ e, the average resolution is $\approx 4.4 \mu\text{m}$ for x_{corr} compared to $\approx 5.2 \mu\text{m}$ for x_{rec} .

For larger θ values the fraction of $cls = 1$ events decreases and the Δx distributions for both x_{rec} and x_{corr} peak at $\Delta x = 0$. Fig. 13 shows that for all θ values an improvement of the resolution of the proposed

method is predicted. However for most angles the effect is small, and precise experimental data are required to see if such an improvement is actually observed.

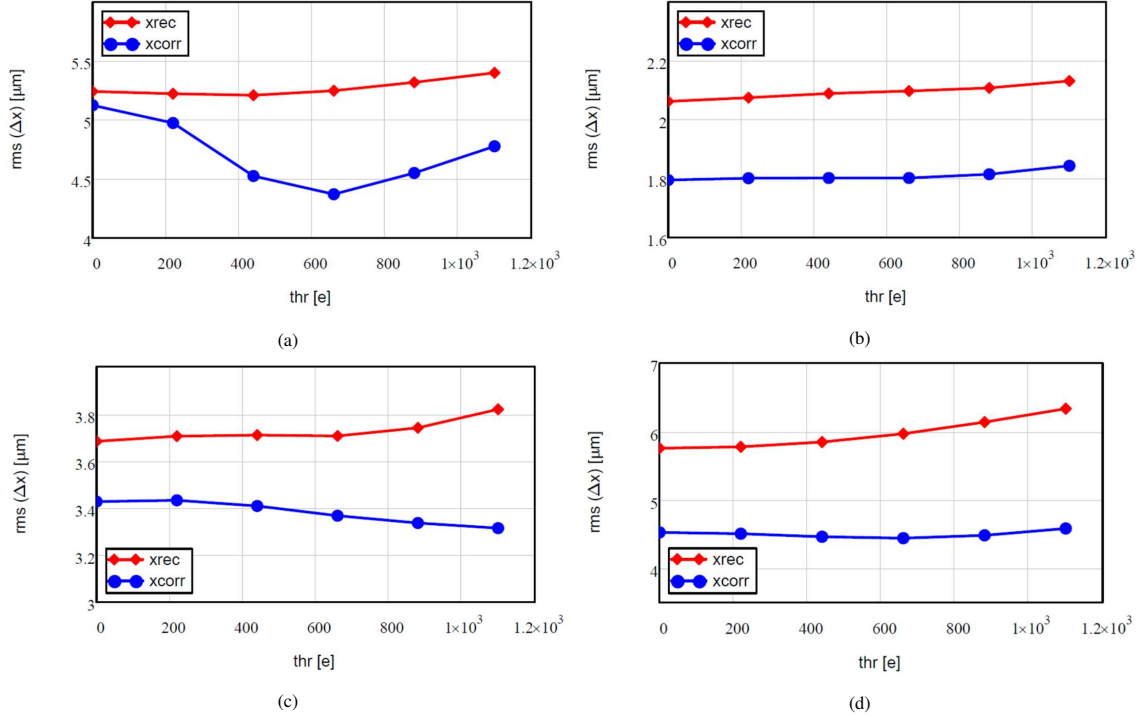


Figure 13: rms widths of the $\Delta x = x_{true} - x$ distributions for $x = x_{rec}$ and $x = x_{corr}$ as a function of thr for (a) $\theta = 0^\circ$, (b) 10° , (c) 20° , and (d) 32° .

The main results of this sections are: For particles with normal incidence, $\theta = 0^\circ$, the proposed method is able to correct the strong bias of the centre-of-gravity algorithm for $cls > 1$ events and significantly improves the overall position resolution. For larger angles θ the bias of the centre-of-gravity algorithm is small. The proposed method is able to correct this bias and predicts minor improvements of the position resolution. This however still has to be demonstrated with experimental data. The proposed method also allows determining the position-response function as a function of reconstructed position. At $\theta = 0^\circ$ this function varies by as much as an order of magnitude, and therefore should be used in track fits. The position response functions have significant non-Gaussian tails and cannot be adequately described by their rms values.

6.2. Comparison of simulation results on cluster size and position resolution to test-beam data

In this section, results of the simulations are compared to test-beam results for silicon pixel sensors under study for the CMS Phase II Upgrade [10, 11, 12, 13, 14, 15]. The data for the comparison are taken from Refs. [11, 12]. The measurements were performed in a 5.6 GeV electron beam [16] at DESY, Hamburg. Three pixel sensors with 150 μm thickness and 25 $\mu\text{m} \times 100 \mu\text{m}$ pixel size were bump-bonded to PSI ROC4Sens chips [17, 18] fabricated on 700 μm thick silicon wafers, and read out with 12 bit resolution. The sensors were operated at $U = 120 \text{ V}$ and at $T = 20^\circ\text{C}$. The distance between the sensors was 2 cm, and they could be rotated together so that the sensor planes remained parallel. The set-up is called "3-Master" (3M). Data for 25 angles, θ , between beam axis and sensor normal from 0° to 30° were recorded. The rotation was around the 100 μm pixel direction. In addition, at $\theta = 8.75^\circ$, data for beam energies between 1.2 and 6 GeV were recorded in order to determine experimentally the influence of multiple scattering on the measured resolution.

The most probable signal from a 5.6 GeV electron at normal incidence is about 11 000 e (elementary charges). In the off-line analysis signals exceeding a threshold of approximately 660 e in contiguous pixels

are grouped into clusters. Signals above threshold in pixels with the same x position (see Fig. 7) are added and counted as one when calculating the cluster size, cls . Fig. 14a shows the measured $\langle cls \rangle$ as a function of θ (label *Test beam*).

The test-beam data are analysed in the following way: The x positions in the three sensors are reconstructed using the centre-of-gravity of the selected pixels, and the distribution of the difference of the position predicted from the outer sensors minus the position measured in the central sensor, Δx_{3M} , is used for determining the position resolution: From the Δx_{3M} distribution the *reduced rms*, $\delta_{\Delta x}$, is calculated iteratively by removing the events with Δx_{3M} values exceeding ± 6 times the *reduced rms*. The measured single detector resolution, which is shown in Fig. 14b (label *Test beam*), is defined as $\sigma_x = \delta_{\Delta x} / \sqrt{1.5}$ [11, 12].

This procedure makes a number of assumptions: The three sensors have the same position resolution, the three position measurements are not correlated, and the shape of the combined response function of two sensors does not differ too much from the one of a single sensor. As discussed in Sect. 2, the centre-of-gravity reconstruction is biased, and the small distances between the detector planes and the small angular spread of the beam effectively result in correlations of the reconstructed positions in the three planes. These effects are most significant at small angles for events with cluster size one in one or more sensors. In addition, only Gauss functions have the property that their convolutions are again Gauss functions. In Sect. 2 it was shown that the response functions of single sensors can be very different from Gauss functions. Multiple scattering too, results in non-Gaussian tails. Nevertheless, it is expected that for angles $\theta \approx \text{atan}(p/d) = 9.5^\circ$ and above, the position resolution can be determined reliably.

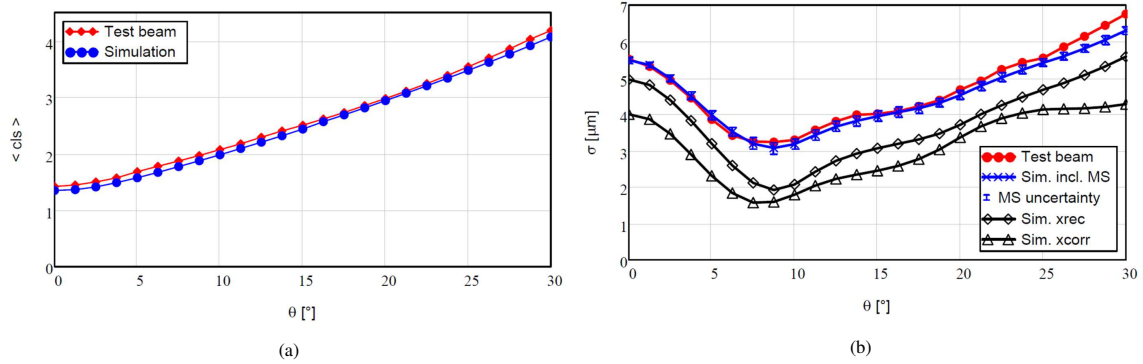


Figure 14: Comparison of simulation with beam-test results for a sensor with 25 μm pitch, 150 μm thickness at a bias voltage $U = 120$ V as a function of angle θ . (a) Mean cluster size, and (b) *reduced rms* of the spatial resolution. Shown are the test-beam results, and for the simulation the reconstructed position using the centre-of-gravity method, x_{rec} , the method proposed in this paper, x_{corr} , and x_{rec} including the effect of multiple scattering in the test-beam set-up.

In order to investigate the effects of multiple Coulomb scattering, data have been taken at the angle with the best resolution, $\theta_{best} = 8.75^\circ$, for energies, E , between 1.6 GeV and 6 GeV and $\sigma_x(E, \theta_{best})$ determined. The straight line extrapolation of $\sigma_x^2(1/E^2)$ to $1/E^2 = 0$ gives $\sigma_{res}(\theta_{best}) = 2.4 \pm 0.1 \mu\text{m}$, the resolution corrected for multiple scattering, and the contribution from multiple scattering of $\sigma_{ms}(5.6 \text{ GeV}, \theta_{best}) = \sqrt{\sigma_x^2 - \sigma_{res}^2} = (2.1 \pm 0.2) \mu\text{m}$. The measured value of $\sigma_x(5.6 \text{ GeV}, \theta_{best}) = 3.2 \pm 0.2 \mu\text{m}$ [11, 12].

In the following, the analysis of the simulated data is described and the results compared to the experimental data. First, using the method described in Appendix A.3, it has been verified that assuming a uniform spatial distribution is valid. For each of the 25 θ values, 5×10^5 events uniformly distributed in the central electrode with pitch $p_x \times p_z$ were simulated as described in Sect. A.1. For the number of pixels, $n_{px} = 3$ has been used for $\theta \leq 15^\circ$, $n_{px} = 5$ for larger angles, and $n_{pz} = 3$ for all angles. The *reduced rms* for the simulated data, σ_{xrec} , obtained with similar cuts as for the experimental data, is shown as a function of θ in Fig. 14b (label Sim. xrec). The relation $\delta_{\Delta x}^2 = 1.5 \cdot \sigma_{xrec}^2 + \sigma_{ms}^2 \cdot (\cos(\theta_{best})/\cos(\theta))^3$ is used for obtaining the *reduced rms* of the simulated residual distributions including multiple scattering. The factor $\sqrt{1.5}$ relates the single sensor resolution with the 3-Master residual distribution. The power 3 takes into account that the angular spread of multiple scattering is approximately proportional to the square root of the path length, and that the residual of the experimental data is determined in the rotated coordinate system of the sensors, whereas for multiple scattering the coordinate system of the beam is relevant. Finally, $\delta_{\Delta x}$

is divided by $\sqrt{1.5}$ for obtaining the simulated resolution including multiple scattering, which is compared in Fig. 14b to the measured resolution.

Up to $\theta = 25^\circ$ the simulation describes the measurement within $0.2\ \mu\text{m}$. At 30° the difference is $0.4\ \mu\text{m}$. This agreement demonstrates the quality of both data and simulation. The figure also compares the simulated resolution for x_{rec} , which uses the centre-of-gravity algorithm, to the one for x_{corr} , the method proposed in this paper. It is seen, that for all angles, however for small angles in particular, a significantly improved resolution is expected, as already discussed in Sect. 6.1.

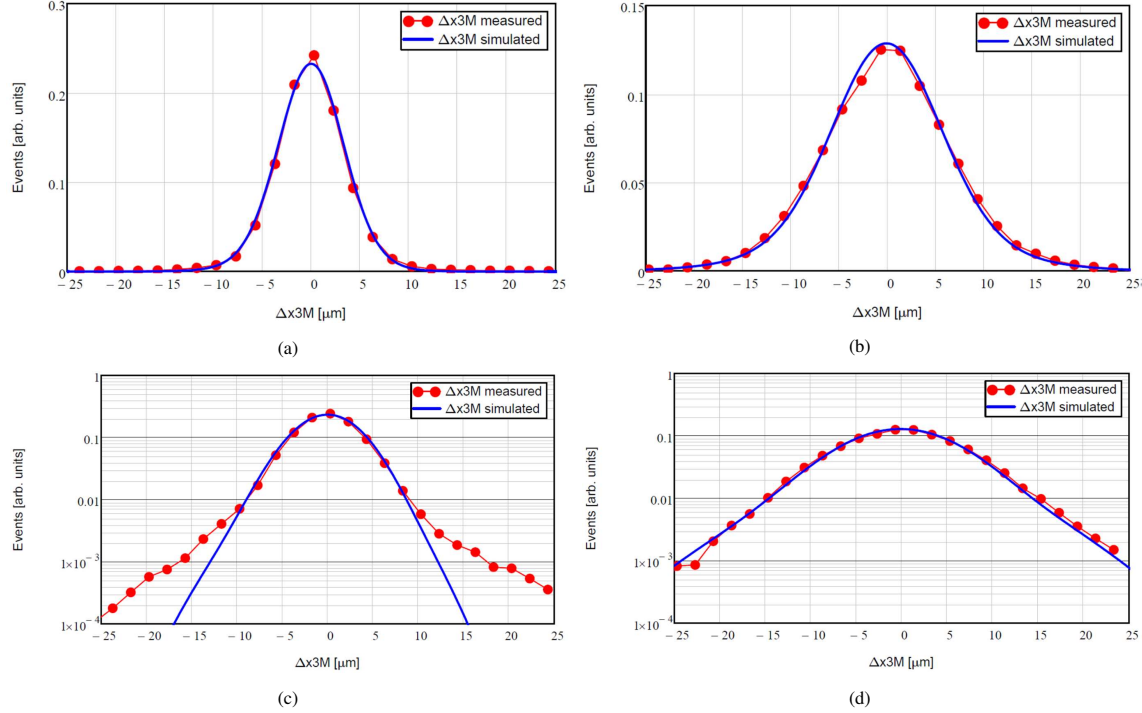


Figure 15: Comparison of the measured to the simulated normalized Δx_{3M} distributions. Δx_{3M} is the difference of the position predicted in the central sensor from the outer sensors minus the position determined in the central sensor, for the set-up with three parallel sensors, for (a) $\theta = 8.75^\circ$ in linear scale, (b) $\theta = 27.5^\circ$ in linear scale, (c) $\theta = 8.75^\circ$ in logarithmic scale, and (d) $\theta = 27.5^\circ$ in logarithmic scale.

In Fig. 15 measured and simulated normalized Δx_{3M} distributions for the data described above are compared for the two angles, $\theta = 8.75^\circ$ and $\theta = 27.5^\circ$. Δx_{3M} is the difference of the position predicted in the central sensor from the outer sensors minus the position determined in the central sensor for the 3M set-up. For the simulated data, the Δx_{3M} distributions are obtained by scaling the Δx values of the simulated response functions $dN/d\Delta x$ (examples are shown in Fig. 12) by the factor $\sqrt{1.5}$, and then convolving the scaled distribution with a Gauss function with $\sigma_{ms}(\theta)$, which accounts for multiple Coulomb scattering. Fig. 15 shows that overall the simulations describe the measured data quite accurately. The deviations for larger $|\Delta x_{3M}|$ seen in Fig. 15c are ascribed to simplifying assumptions in the analysis of the data from three detector planes and to the use of a Gauss function for multiple scattering, which ignores large-angle scattering events.

As discussed in Sect. 2, at small angles θ the reconstructed positions in the three sensors are correlated because of the bias of the centre-of-gravity method. As a result the Δx_{3M} distribution shows narrow peaks [11], mainly but not only from events with cluster size one in one, or more than one sensor. The simulation of the Δx_{3M} distribution at small angles requires the knowledge of the relative alignment of the three sensors with an accuracy of $\lesssim 1\ \mu\text{m}$.

The main results of the comparison of simulation results with test-beam data for angles θ between 0° and 30° presented in this section are: The average cluster sizes agree to better than 0.1, and the *reduced rms* of the measured sensor resolution, which includes the effects of multiple scattering, agrees within $0.2\ \mu\text{m}$ up to 25° , and the central parts of the measured Δx_{3M} distributions are well described.

7. Summary and conclusions

The topic of the paper is the position reconstruction of signals from segmented detectors. It is shown that the frequently used centre-of-gravity method can result in a strong bias of the reconstructed position. The bias is particularly strong if the width of the signal distribution at the position of the read-out electrodes is less than their size. For events with signals in more than one read-out electrode, a method is presented which corrects the bias of the centre-of-gravity method. With the help of simulated events a significant improvement of the position resolution is demonstrated for charged particles traversing with different angles a pixel sensor with a pixel pitch of $25\ \mu\text{m} \times 100\ \mu\text{m}$. In addition to improving the position resolution, the method provides an estimate of the position-response function for every reconstructed event. As the response function depends strongly on the position of the particle relative to the electrodes, it should be used for track fits. The proposed method does not achieve a higher precision than previously used methods, but it is more easily implemented and does not require additional information beyond the signals recorded in the individual detector elements. It can also be applied to other reconstruction methods than the centre-of-gravity algorithm, and for the position reconstruction in other types of segmented detectors, like calorimeters.

As a next step, the method should be applied to experimental data for silicon sensors without and with radiation damage in order to confirm the improvement predicted from the simulated events. In addition, the proposed method can be applied to other position reconstruction methods, like the *head-tail* algorithm. Also the use of the method for other detectors is strongly encouraged.

As a by-product, a simulation program for silicon pixel sensors has been developed. With the program about 500 k events per minute can be simulated for silicon pixel sensors with 100 % charge collection. It has been verified that the generated events provide an accurate description of test-beam data. Missing in the program are the effects of energetic δ electrons and the Lorentz drift in magnetic fields, which however can be implemented. Last but not least, the program can be extended to the simulation of radiation-damaged silicon sensors with losses of charge carriers during their drift in the sensor. This however, requires the knowledge of the electric field, the position-dependent trapping probabilities separately for electrons and holes, and the weighting field for radiation-damaged sensors.

A. Appendices

A.1. Signal simulation

This Appendix gives details of the program presented in Sect. 4 for simulating the signals produced by energetic charged particles in a silicon pixel sensor with 100 % charge collection. The aim is to have a flexible program which is fairly realistic and which can generate 500 k events in about 1 minute on a standard PC. Fig. 7 of Sect. 4 displays the cross section and the top view of the simulated pixel sensor, defines the coordinate system and shows a track traversing the sensor in the $x - y$ plane with the angle θ relative to the y axis. Table 1 lists the parameters used in the simulation.

For a pad sensor of thickness d , p -doping density, N_d , the n^+p junction at $y = d/2$, and bias voltage U , the absolute value of the electric field above full depletion is approximately

$$E_y(y) = U/d + y \cdot q_0 \cdot N_d / \epsilon_{Si}, \quad (3)$$

with the elementary charge q_0 , the dielectric constant of silicon, ϵ_{Si} ², and the coordinate system shown in Fig. 7. This only approximates the electric field of a sensor with segmented electrodes. Close to the electrodes the electric field is more complicated and depends on a number of parameters: the width of the pixel implants, the doping of the bulk and of the p^+ implants required to electrically separate the electrodes, the boundary conditions on the SiO_2 surface in-between the electrodes, and the dark current. The charge sharing between electrodes for charges generated at x values close to their boundaries is influenced by this field distribution. A study of the charge collection close to the sensor surface is reported in Ref. [19], with the conclusion that even in non-radiation damaged sensors the electric field close to the electrodes is only poorly known as important information required for TCAD simulations is lacking.

²The value 11.7 has been assumed for the relative dielectric constant of silicon.

Symbol	Value	Description
d	150 μm	Sensor thickness
n_{px}	3, 5, 7	Number of pixels in x direction
n_{pz}	3	Number of pixels in z direction
p_x	25 μm	Pixel pitch in x direction
p_z	100 μm	Pixel pitch in z direction
n_y	15, 30	Number of y -steps for energy loss
$\Delta x_{min}, \Delta z_{min}$	2 μm	see text
N_d	$4.5 \times 10^{12} \text{cm}^{-3}$	p -doping density
U	120, 150 V	Bias voltage
T	20 $^\circ\text{C}$	Temperature
x_{true}	$-p_x/2 \leq x_{true} < p_x/2$	x position of track at $y = 0$
z_{true}	$-p_z/2 \leq z_{true} < p_z/2$	z position of track at $y = 0$
θ	0 $^\circ$ to 30 $^\circ$	Particle angle relative to y axis
MPV	11 000 e	Most probable charge for $\theta = 0^\circ$
ΔE_{max}	2.0	Maximal charge / MPV

Table 1: Input parameters used in the simulation program.

Next, the simulation of the e - h pairs and the charges Q induced in the electrodes by a particle traversing the sensor at position $(x_{true}, 0, z_{true})$ at an angle θ to the y axis is presented. In order to take into account the local energy-loss fluctuations, the sensor depth is divided into n_y segments of depth $\Delta y = d/n_y$. For every Δy interval a random number for the energy loss ΔE is generated for the particle-path length $\Delta y/\cos(\theta)$ as described in Ref. [9] and Appendix A.2.

An electron cloud with the distribution $\delta(x) \cdot \delta(z)$ at $y = y_0$, diffuses to a 2-D Gaussian charge distribution when drifting to $y = d/2$ with the variance

$$\sigma^2(y_0) = \frac{2 k_B T}{q_0} \int_{y_0}^{d/2} \frac{dy}{E_y(y)}, \quad (4)$$

with the Boltzmann constant k_B , and the absolute temperature T . It is remarkable that $\sigma(y_0)$ does not depend on the mobility, which significantly simplifies the simulation. This follows from

$$\sigma^2(\tau) = \frac{2 k_B T}{q_0} \mu_e \cdot \tau \Rightarrow \frac{d\sigma^2}{d\tau} = \frac{2 k_B T}{q_0} \mu_e \Rightarrow \frac{d\sigma^2}{dy} = \frac{d\sigma^2}{d\tau} \frac{d\tau}{dy} = \frac{2 k_B T}{q_0 E_y(y)},$$

where the symbol τ is used for time. For $E = 0$, which however does not occur in a real sensor, the expression of Eq. 4 is not defined, and $\sigma^2(\tau) = 2 \cdot k_B \cdot T \cdot \mu_{e/h} \cdot \tau/q_0$ has to be used.

Inclined tracks in the x - y plane traversing a distance Δy cover an x range of width $\Delta x = \Delta y \cdot |\tan(\theta)|$, which is taken into account by convolving the Gauss distributions with a box distribution of width $\Delta x' = \max(\Delta x, \Delta x_{min})$. In z , the Gauss distribution is convolved with a box distribution of width Δz_{min} . The convolved Gauss distribution of a charge cloud drifting from $(0, y_0, 0)$ to $y = d/2$ is denoted $G^*(x, y = d/2, z; y_0)$. The parameters Δx_{min} and Δz_{min} , which are only relevant for the charges produced close to the electrode boundaries, are introduced to describe the transverse width of the initial charge carrier distribution and the effects of charge sharing due to the electric field in the region of the electrode boundaries. The choice $\Delta x_{min} = \Delta z_{min} = 2 \mu\text{m}$ is quite arbitrary, but the exact value hardly influences the results. The charge induced in a given electrode is obtained from

$$Q_i = \sum_{iy=1}^{n_y} \int_{pixel} G^*(x = x_{true} + y_{iy} \cdot \tan(\theta), y = d/2, z = z_{true}; y_{iy}) dx dz. \quad (5)$$

To speed up the simulation, the n_y cumulative distributions of the different G^* functions are calculated only once for a given angle θ .

The effect of fluctuations in the charge cloud during its drift has been estimated using multinomial distributions, which describe the fluctuations of the signals in individual electrodes for a given total signal.

For the 150 μm thick sensors investigated, the number of charge carriers generated by energetic particles (MPV $\approx 11\,000\text{e}$) is sufficiently large compared to the *rms* noise of 250 e, so that this effect can be neglected. However, this is not the case for thin detectors with low electronics noise.

Energetic δ electrons which travel a finite distance and thus change the shape of the generated charge distribution, are so far not implemented in the simulation. Therefore, the results of the simulation become unreliable for charge values exceeding ≈ 2 times the most probable one.

In a further analysis step, the electronics noise is simulated by adding a Gaussian-distributed random number to every Q_i , threshold cuts are made, the cluster size is calculated and the x and z positions reconstructed as discussed in the main part of the paper.

A.2. Energy loss simulation

This Appendix describes the method used to generate random numbers for the energy loss, ΔE , of energetic charged particles traversing a distance t in silicon. This is achieved by the following steps, most of which are described in detail in Ref. [9].

1. The mean number of energy-loss interactions of a particle traversing the distance t is $\mu = t/t_1$, where t_1 is the mean spatial distance between energy-loss events.
2. The ΔE distribution for n energy-loss events, $dP^{(n)}(\Delta E)/d\Delta E$, is obtained by the $n - 1$ -fold convolution of the single-event ΔE distribution $dP^{(1)}(\Delta E)/d\Delta E$. For $n = 0$, $dP^{(0)}(\Delta E)/d\Delta E = \delta(\Delta E)$.
3. The ΔE distribution for the distance t is calculated as the sum over the $dP^{(n)}(\Delta E)/d\Delta E$ distributions weighted with the Poisson distribution with mean μ : $dP(\Delta E)/d\Delta E = \sum_{n=0}^{\infty} ((\mu^n/n!) \cdot e^{-\mu} \cdot (dP^{(n)}(\Delta E)/d\Delta E))$.
4. The inverse of the normalised cumulative distribution of $dP(\Delta E)/d\Delta E$ is used to generate random numbers for the energy loss ΔE of particles passing the distance t in silicon.

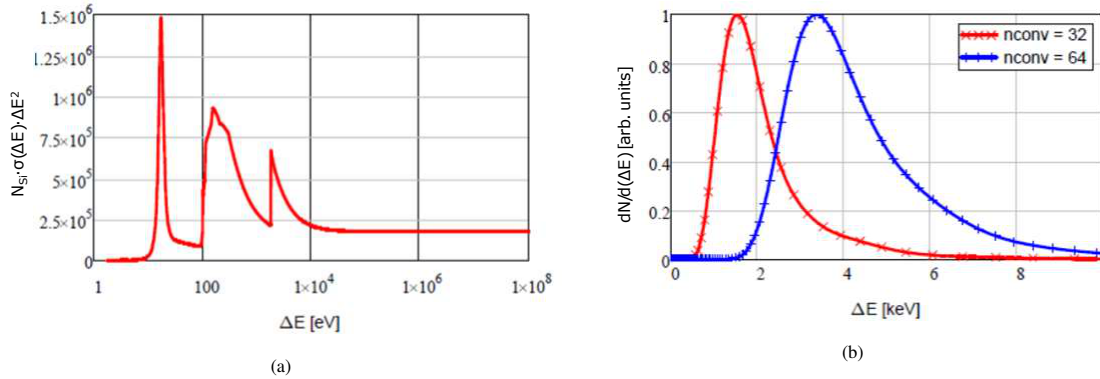


Figure 16: (a) Differential cross section for a single energy-loss event, $d\sigma^{(1)}(\Delta E)/d\Delta E$ of 5 GeV/c pions in silicon multiplied by N_{Si} , the number of Si atoms per unit volume, and ΔE^2 . (b) ΔE distribution for 32 (64) energy-loss events obtained by convolving $d\sigma^{(1)}(\Delta E)/d\Delta E$ 32 (64) times. The curves are normalised to 1 at their maxima. The mean distance between energy-loss events calculated using the data shown in (a) is 0.2602 μm , and 32 (64) convolutions correspond to a path length of 8.33 (16.65) μm .

A program for calculating the ΔE distribution for a single energy-loss event based on Ref. [9] is available at Ref. [20], where also $N_{Si} \cdot \Delta E^2 \cdot d\sigma^{(1)}(\Delta E)/d\Delta E$ for 5 GeV/c pions for the ΔE range from 1.796 eV to 174.2 MeV in 1699 logarithmic ΔE bins can be accessed. Fig. 16a shows these data. $N_{Si} = 4.99 \times 10^{22} \text{cm}^{-3}$ is the number of Si atoms per cm^{-3} . The differential cross section multiplied by ΔE^2 is shown because of the $1/\Delta E^2$ dependence of the Rutherford cross section. The structures below 10 keV reflect the atomic structure of Si and the constant at higher ΔE the Rutherford formula. $N_{Si} \cdot d\sigma^{(1)}(\Delta E)/d\Delta E \cdot d\Delta E$ is the inverse of the mean distance of events with an energy loss between ΔE and $\Delta E + d\Delta E$, and its integral is $1/t_1$, the inverse of the mean distance between energy-loss events; For the data of Fig. 16a, $t_1 = 0.2602 \mu\text{m}$.

The convolved spectrum $h(f, g)$ of two data sets (t_i, f_i) and (t_i, g_i) with bin widths Δt_i is obtained by

$$h_j = \sum_{i=0}^j (\Delta t_i \cdot f_i \cdot g(t = t_j - t_i)), \quad (6)$$

where for $g(t)$ a linear interpolation between the g_i values is used. The differential cross sections for n energy-loss events are

$$\frac{d\sigma^{(n)}(\Delta E)}{d\Delta E} = \begin{cases} \delta(\Delta E) & \text{for } n = 0 \\ h(d\sigma^{(1)}/d\Delta E, d\sigma^{(n-1)}/d\Delta E) & \text{for } n \geq 1. \end{cases} \quad (7)$$

For $n = 0$, no energy is lost, for $n = 1$, the energy-loss cross section is the single-event energy-loss cross section, and for $n > 1$, the cross section is calculated iteratively using the convolution of Eq. 6.

Next, the mean number of energy-loss events $\mu = \Delta t/t_1$ for the path length $\Delta t = \Delta y/\cos(\theta)$ is calculated, and the probability density $dP/d\Delta E$ is obtained from the Poisson-weighted sum

$$\frac{dP}{d\Delta E} = \sum_{n=0}^{\infty} \frac{\mu^n \cdot e^{-\mu}}{n!} \cdot \frac{dP^{(n)}}{d\Delta E} \cdot \left(\frac{\mu^n \cdot e^{-\mu}}{n!} \cdot \frac{dP^{(n)}}{d\Delta E} \right). \quad (8)$$

The functions $dP^{(n)}/d\Delta E$ are the normalised cross sections $d\sigma^{(n)}/d\Delta E$, and $dP/d\Delta E$ the energy-loss probability density for the path length Δt .

For generating $dP/d\Delta E$ -distributed random numbers ΔE_i , the standard method using the probability distribution $P(\Delta E) = \int_0^{\Delta E} (dP/d\xi \cdot d\xi)$ is followed. A random number, r_i , which is uniformly distributed between 0 and 1 is generated and $\Delta E_i = P^{(-1)}(r_i)$, where $P^{(-1)}$ is the inverse of $P(\Delta E)$.

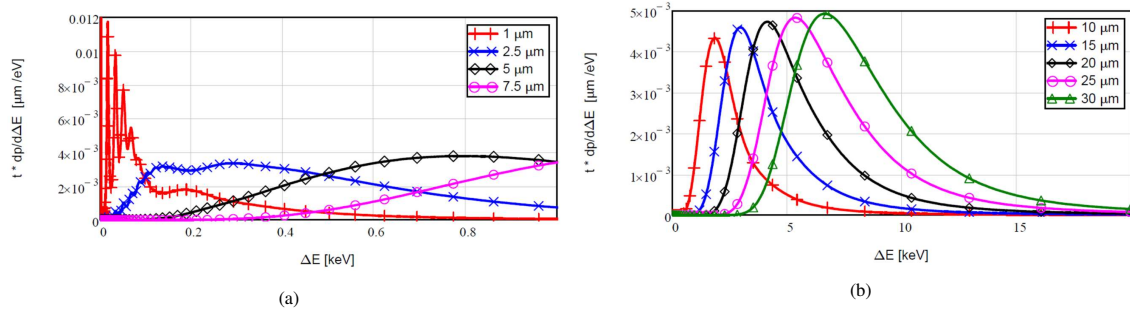


Figure 17: Product of the Si-path length t and the probability density function $dP/d\Delta E$ for different t for 10^6 Monte Carlo events each. (a) t range $1 \mu\text{m}$ to $7.5 \mu\text{m}$, and (b) t range $10 \mu\text{m}$ to $30 \mu\text{m}$.

Fig. 17 shows for 10^6 generated events the product $t \cdot dP/d\Delta E$ for several Si-path lengths, t . As the mean $\langle \Delta E \rangle \propto t$, $dP/d\Delta E$ is multiplied with t for visibility reasons. For $t = 1 \mu\text{m}$, which corresponds to an average of 4 energy-loss events, the structures caused by the single energy-loss cross sections are visible, and there is also a significant number of $\Delta E = 0$ events. For $t \gtrsim 5 \mu\text{m}$ the structure disappears, the fraction of $\Delta E = 0$ events is negligible and the probability density distribution approaches a Landau curve. One also notices, that at the most probably value $t \cdot dP/d\Delta E$ increases with t , which is caused by the decrease of the relative width with t . For the simulation of the detector response in Sect. 6 the t range is $15 \mu\text{m}$ to $20 \mu\text{m}$.

A.3. Spatial distribution of tracks over the electrode pitch

For the simulations and the correction method a uniform $d^2N/(dx_{true}dz_{true})$ distribution is assumed. In addition, it is stated that if this is not the case, the cumulative distribution will deviate from a straight line, however, the method sketched in Fig. 2b can still be applied. In this Appendix a method for determining dN/dx_{true} and dN/dz_{true} from the measured spatial distribution of the particles over the sensor, is described.

The measured 1D-spatial distribution is given by a histogram with n bins (Nb_i, xb_i), where Nb_i is the number of events in the bin centred at position xb_i ; b stands for *beam*, as such measurements are typically performed in test beams. For simplicity the xb_i are assumed to be uniformly spaced, with spacing Δxb . Next, it is assumed that the event numbers per Δxb inside the individual bins can be obtained by a linear interpolation, which gives for bins $i = 2$ to $n-1$:

$$Nb(\xi^{(i)}) \approx Nb_i + \frac{Nb_{i+1} - Nb_{i-1}}{2 \cdot \Delta xb} \cdot \xi^{(i)} \quad \text{for} \quad -\Delta xb/2 \leq \xi^{(i)} < \Delta xb/2, \quad (9)$$

where $\xi^{(i)}$ is the distance from the bin centre. Ignoring a minor corrections for the edge bins, the sum over all bins is

$$Nb(\xi) \approx \sum_{i=1}^n Nb(\xi^{(i)}) = N_{tot} + \frac{Nb_n - Nb_1}{2 \cdot \Delta xb} \cdot \xi, \quad (10)$$

with the total number of events N_{tot} . From this follows the mean probability density distribution for the electrodes of pitch p

$$dP(x)/dx \approx \frac{1}{p} \cdot \left(1 + \frac{Nb_n - Nb_1}{2 \cdot N_{tot} \cdot \Delta xb} \cdot x\right) \quad \text{for} \quad -p/2 \leq x \leq p/2. \quad (11)$$

For the data discussed in Sect. 6.2, typical values of the x slope are a few 10^{-3} cm^{-1} , which justifies the assumption of a uniform dN/dx_{true} distribution for the simulation and a linear cumulative distribution for the correction of x_{rec} . It also implies that the linear interpolation used in Eq. 9 is adequate.

Acknowledgements

We acknowledge the support of A. Ebrahimi and F. Feindt by the BMBF, the German Federal Ministry of Education and Research, funding code 05H19GUCC9, and of I. Zoi by the Emmy-Noether program (HI 1952/1-1) of the DFG, the German Research Foundation. We thank D. Dannheim for valuable comments to a preliminary version of the paper.

References

References

- [1] E. Belau et al., *Charge collection in silicon strip detectors*, Nucl. Instr. & Methods 214 (1983) 253–260.
- [2] G. Landi and G.E. Landi, *Probability Distributions of Positioning Errors for some Forms of Center-of-Gravity Algorithms. Part II*, arXiv:2011.14474 (Nov. 2020), and references therein to several papers by the same authors.
- [3] R. Turchetta, *Spatial resolution of microstrip detectors*, Nucl. Instr. & Methods A 335 (1993) 44–58.
- [4] R. Bugiel et al., *High spatial resolution monolithic pixel detector in SOI technology*, Nucl. Instr. & Methods A 988 (2021) 164897.
- [5] I. Gorelov et al., *A measurement of Lorentz angle and spatial resolution of radiation hard pixel sensors*, Nucl. Instr. & Methods A 481 (2002) 204–222.
- [6] K. Akiba et al., *Charged particle tracking with the Timepix ASIC*, Nucl. Instr. & Methods A 661 (2012) 31–49.
- [7] D. Dannheim et al., *Combining TCAD and Monte Carlo methods to simulate CMOS pixel sensors with small collection electrode using the Allpix² framework*, Nucl. Instr. & Methods A 964 (2020) 163784.
- [8] D. Dannheim et al., *Corryvreckan: a modular 4D track reconstruction and analysis software for test beam data*, JINST16 (2021) P03008.
- [9] H. Bichsel, *Straggling in thin silicon detectors*, Review of Modern Physics, Vol. 60-3 (1988) 663–699.
- [10] CMS Collaboration, *The Phase-2 Upgrade of the CMS Tracker*, Technical Design Report, CERN-LHHC-2017-009, CMS-TDR-17-001.
- [11] I. Zoi, *Search for diboson resonances in the all jets final state with CMS and pixel sensors development for HL-LHC*, PhD thesis, University of Hamburg - in progress.
- [12] A. Ebrahimi, et al., *Position resolution with 25 μm pitch pixel sensors before and after irradiation*, submitted for publication to Nucl. Instr. & Methods A, arXiv:2107.0464.

- [13] F. Feindt, *Silicon Pixel Sensors in the Inner Tracking System of the CMS Experiment*, PhD thesis, University of Hamburg - in progress.
- [14] J. Schwandt, *CMS Pixel detector development for the HL-LHC*, Nucl. Instr. & Methods A 924 (2018) 59–63.
- [15] G. Steinbrück for the CMS Tracker Group, *Development of planar pixel sensors for the CMS Inner Tracker at the High-Luminosity LHC*, Nucl. Instr. & Methods A 978 (2020) 164438.
- [16] R. Diener et al., *The DESY II test beam facility*, Nucl. Instr. & Methods A 922 (2019) 265–286.
- [17] S. Wiederkehr, *The Effective Lifetime of $B_s^0 \rightarrow \mu \mu$ and Designing a Readout Chip for Pixel Sensor Development*, PhD thesis, ETH Zürich, 2018, www.research-collection.ethz.ch/handle/20.500.11850/314130.
- [18] T. Rohe et al., *ROC4Sens – a generic readout chip for sensor studies*, 31st RD50 workshop, CERN, Geneva, Nov. 20–22, 2017, <https://indico.cern.ch/event/663851/contributions/2788211/>.
- [19] T. Poehlsen et al., *Charge losses in segmented silicon sensors at the Si–SiO₂ interface*, Nucl. Instr. & Methods A 700 (2013) 22–39.
- [20] The original code by H. Bichsel: https://www.slac.stanford.edu/~sudong/silicon/bichsel_covfold.tar and a Fortran90 code: <https://github.com/pitzl/bichsel>, where also a number of spectra can be found.